Visualisation and numerical analysis of laser powder bed fusion under cross-flow

Visualisation and numerical analysis of laser powder bed fusion under cross-flow

I. Bitharas, A. Burton, A.J. Ross, A.J. Moore

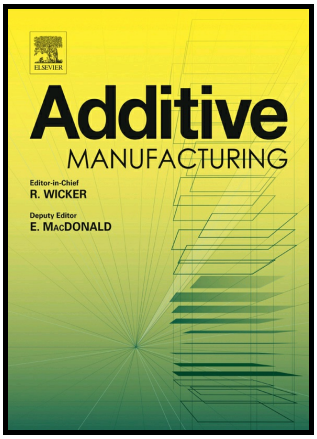

PII: S2214-8604(20)31062-9

DOI: https://doi.org/10.1016/j.addma.2020.101690

Reference: ADDMA101690

To appear in: *Additive Manufacturing*

Received date: 11 June 2020
Revised date: 5 October 2020
Accepted date: 29 October 2020

Please cite this article as: I. Bitharas, A. Burton, A.J. Ross and A.J. Moore, Visualisation and numerical analysis of laser powder bed fusion under cross-flow, *Additive Manufacturing,* (2020) doi:https://doi.org/10.1016/j.addma.2020.101690

Visualisation and numerical analysis of laser powder bed fusion under cross-flow

I. Bitharas, A. Burton , A. J. Ross and A. J. Moore

Institute of Photonics and Quantum Sciences, Heriot-Watt University, Edinburgh, EH14 4AS, UK

Abstract:

As well as preventing oxidation, a cross-flow of inert gas over the powder bed extracts process by-products, making it critical for process repeatability and build quality during the additive manufacturing of metallic parts. In this study, high-magnification schlieren imaging was employed to visualise the interactions between the cross-flow, laser plume and individual powder particles for the first time. Novel 3D multiphysics simulations of the cross-flow, including the vapour jet and laser plume, were used to calculate energy, momentum and species transport over the processed area in order to understand and quantify the observed interactions. During processing, metallic fumes as well as a significant number of airborne powder particles and agglomerates were observed to remain close to the powder bed, over the scanned area. These particles interact in a range of stochastic collisions that affect the build consistency. Refractive index gradients were formed in the atmosphere above the island scans, which extended many tens of mm beyond the processing area. The rate of extraction of these by-products, regulated by the velocity of the cross-flow, was related to the quality of the builds. A cross-flow perpendicular to the laser scan direction was observed to remove airborne particles from adjacent laser scans most effectively, limiting laser-particle and particle-particle interactions. The model demonstrated that the refractive index gradients away from the vapour jet are due to the metal concentration rather than the temperature of the heated gas.

Keywords:

High-speed imaging; Schlieren imaging; Powder consolidation; Theory and modelling (kinetics, transport, diffusion); Cross-flows

1. Introduction

Laser powder bed fusion (LPBF) is the most widely adopted process for the additive manufacture (AM) of metallic components. Its continuous improvement is underpinned by rigorous scientific research, allowing increased understanding of this multifaceted process. Despite the developments in this technology, issues such as reduced fatigue life [1] and inconsistent part quality [2] are hindering its widespread adoption. A key component of the LPBF process, critical for its repeatability and stable operation, is the cross-flow of inert gas over the powder bed, which allows the removal of metallic vapours, fumes and airborne particles from the immediate area being processed.

A number of studies present measurements and numerical models of the flow conditions in commercial chambers, correlating their results with the quality of the built parts. Ferrar et al. [3] found that lower porosity specimens with higher compressive strength could be manufactured when the Ar flow was more uniform across the powder bed. Ladewig et al. [4] correlated low velocity zones in the cross-flow with the appearance of process defects such as lack of fusion or balling. Anwar et al. [5] showed that in addition to the location on the powder bed, the direction of laser scanning with regards to that of the cross-flow played a role in the production of spatter. When scanning with the flow, printed specimens had 10% higher ultimate tensile strength (UTS) compared to those printed whilst scanning counter to the flow. Philo et al. [6] used CFD simulations to solve for the fluid dynamics of the cross-flow, neglecting temperature effects and metal vapour transport, to show that recirculations within the chamber can disrupt the flow locally, adversely affecting the extraction of process by-products. A similar CFD model was used by Anwar et al. [7] to trace the motion of large spatter particles under cross-flow. Their simulations and measurements suggested that the majority of ejected particles did not accumulate enough momentum to reach the cross-flow outlet from the chamber.

Most recently, Reijonen et al. [8] found that insufficient momentum in the cross-flow resulted in parts with increased porosity and scan tracks with wider melt pools with lower penetration. Laser light scattering by the metal vapour, refraction of the laser beam due to density gradients and increased frequency of laser-particle interactions were identified as possible causes. Early work in YAG laser welding by Matsunawa et al. [9] showed that metallic nanoparticles at the plume's periphery caused significant reduction of the energy incident on the surface due to Rayleigh scattering. For fibre laser welding operating at 1070 nm, ~10% of the total laser power has been estimated to attenuate due to scattering mechanisms [10,11], a fraction that varies depending on the temperature, size distribution and concentration of the particles. In addition, the transient nature of the vapour plume and the constant motion of the laser beam results in additional variation of the total power and beam quality that reaches the melt pool. Reports of inconsistent penetration and inhomogeneous tracks for laser PBF when operating with a low flowrate [4], as well as increased penetration at reduced atmospheric pressure [12] and reduced penetration at high atmospheric pressure [13], are all consistent with these observations.

A great deal of information is revealed via process observation, although little of this research to date has involved the cross-flow. Matthews et al. [14] showed that the vapour jet produced by the laser causes a flow which entrains the surrounding particles, denuding the powder bed. Bidare, Bitharas, et al. [15], used schlieren imaging to visualise the laser plume and cross-flow in PBF for two different process settings. It was shown that the total momentum in the plume, which increased exponentially with laser power, is a determining factor in how well the condensed vapour and ejected particles can be extracted for a given flowrate. However, the magnification of the schlieren system was not sufficient to resolve individual powder particles: only the trail from hot ejected particles could be observed, meaning that the detail of the particle interaction with the laser beam and cross-flow was lost.

This paper presents a visualisation study of the interaction between the cross-flow, laser plume and ejected particles during the LPBF manufacture under steady build conditions, which has not been observed previously. High-magnification schlieren and direct imaging allowed a clear view into the powder bed and the atmosphere above it. Additionally, a 3D multiphysics numerical model of the laser plume and cross-flow within an inert atmosphere is utilised to simulate vapour concentrations and temperature distributions above the powder bed. Relevant literature is discussed in the context of the visualised phenomena.

2. Experimental setup

We used an open architecture LPBF system, designed for in-situ measurements [16]. The main advantage of the system is that it allows easy access to optical diagnostics without compromising its ability to produce small scale parts. An important feature of the system is that experiments are not restricted to single tracks or islands within the first layer, so that realistic build conditions can be captured. This section describes aspects of the system that are relevant to this paper and that have not been reported previously: the characteristics of the cross-flow system and a high-magnification schlieren system capable of imaging individual cold particles.

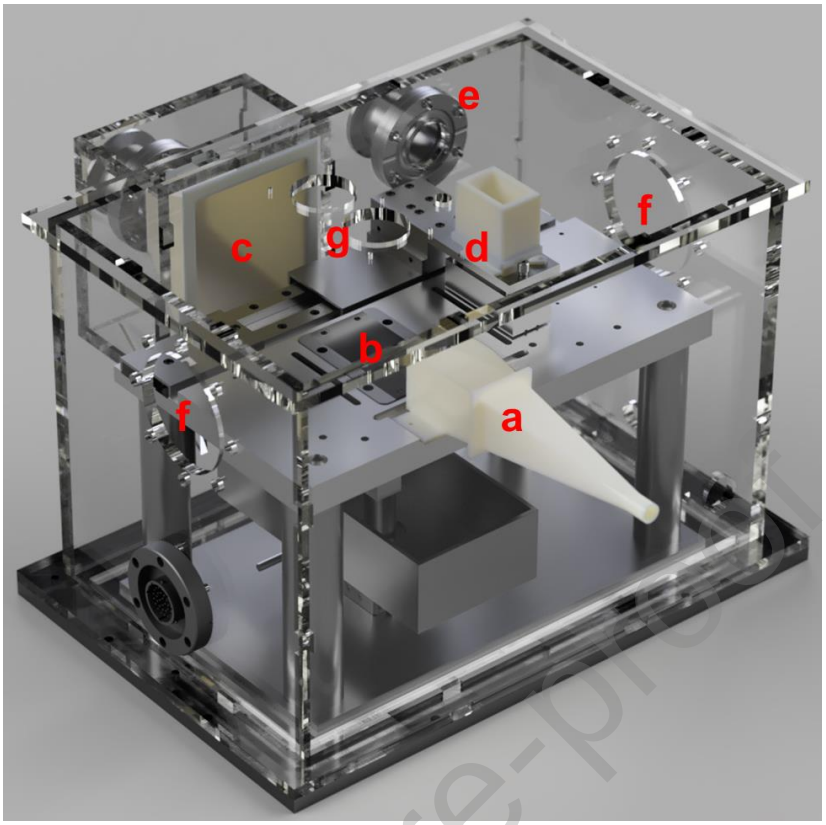

Fig. 1 CAD render of the open-architecture laser PBF system. a) Cross-flow device; b) Build plate (coupon); c) Cross-flow outlet; d) Powder hopper and spreader; e) O_2 sensor port; Apertures for f) schlieren windows and g) laser & direct imaging windows. These windows are omitted from the render so as not to obscure other components.

2.1 Cross-flow

The layout of the open architecture system is shown in Fig. 1. The cross-flow inlet was designed to provide a laminar gas flow over the build plate during processing while channelling relatively large volumetric flowrates of gas. To achieve this, principles of welding torch trailing shield design [17] as well as subsonic wind tunnel design [18] were followed. A diffusor, labelled 'a' in Fig. 1, was used to expand the flow from the 8 mm diameter of the supply pipe to a 40 x 40 mm^2 square inside the build chamber. An angle of ~6^o on the diffusor walls prevented separation of the boundary layer. Following that, the expanded flow was conditioned further by passing through a honeycomb structure, settling chamber and mesh screen before entering the LPBF chamber. Argon shielding gas (Argoshield pure, BOC gases) was supplied directly to the diffusor from a compressed gas cylinder both for purging the chamber prior to a build and for generating the cross-flow during the build experiments.

The cross-flow outlet was positioned on the chamber wall opposite the inlet. It was connected to an exhaust pipe venting to the atmosphere via a stack of P3 filters. The pressure in the chamber was therefore approximately 1 bar (absolute pressure). The O_2 level was measured in the chamber using a lambda sensor (Nitron Microx ZiO_2). The chamber was sufficiently air-tight that less than 2 ppm O_2, the detector's lower limit, were measured over a 24-hour period in a static Ar atmosphere after initial purging of the chamber. During processing with a constant flow of Ar over the bed, the atmosphere was always less than 50 ppm of O_2, and significantly below that for most of the time.

The cross-flow over the bed was characterised in a set of separate experiments. The peak flow velocity at the midpoint of the build plate on the centre-line of the cross-flow inlet diffusor (~20 mm above the build plate) was measured by high-speed imaging of tracer particles within the flow, observed through the schlieren windows. Based on these measurements, two cross-flow speeds were used in this study: 1.2 m/s (referred to as the low flow condition in the text) and 2.1 m/s (high flow condition). Due to the relatively small build area (the build plate coupon is 80 x 40 mm^2) the flow speed and its distribution were considered constant across it, validated by the numerical

modelling described later. No turbulence could be detected in the cross-flow with the schlieren system set at its highest contrast sensitivity of ~1 arcsecond.

2.2 High-magnification schlieren and direct imaging

In our previous work, a Z-type schlieren system was used [13,15], originally developed to visualise shielding gas flows in arc welding [19]. That system used long focal length concave mirrors to reduce optical aberrations [20] whilst maintaining a relatively large field of view and high contrast sensitivity. To overcome the limited magnification and large size of that system, a high-resolution lens-based schlieren system was developed for laser PBF, as proposed by Vogel et al. [21] for the observation of ablation dynamics. A collimated beam was produced by a circular aperture of diameter ~150 µm illuminated by a high-power LED (SOLA-SM) to provide a point-like source in the focal plane of the input lens (SMC Pentax-A 50 mm F1.7). Schlieren windows (λ/4 flatness) on the ends of the chamber allowed the light to traverse the build area, being collected by an analyser lens (Sigma DL 75-300 mm) that focused the beam containing the flow information back to a point. A vertical, solid knife-edge was positioned with a micrometer stage at the focal point, blocking 50% of the image. Schlieren images in which the intensity was proportional to the refractive index gradient $\partial n/\partial x$ were produced in this manner. A telephoto lens (Sigma 150-600 mm f/5-6.3) was focussed through the analyser to produce a virtual image of the measurement plane inside the PBF chamber. These images were recorded with a Photron Fastcam Mini AX200 monochrome camera at 21,600 fps and 384 × 384 pixels. The focusing lens was adjusted to a field of view of roughly 6 x 6 mm^2, so that 5 x 5 mm^2 island scans were fully visible. A short-pass filter (Schott KG-5) and polariser were included in the setup. Direct imaging from above the powder bed (10,000 fps at 768 x 528 pixels) was also undertaken through the top viewing window, as detailed in [12,13,15].

The Fastcam Mini's sensor captures the image intensity information in 12 bits, while the software stores 16-bit images. For display, the saved images were contrast-stretched so that ~3% of the pixels were saturated, before being converted to 8-bit format. Additionally, for any high-sensitivity schlieren system, small imperfections and slight soiling of the optics degrade image quality, an effect which is more pronounced when using lenses rather than the concave mirrors. Therefore, the background of the images was removed by dividing each image by a tare image that contained no flow information recorded at the beginning of each sequence, prior to contrast stretching.

2.3 PBF build experiments

Gas-atomized stainless steel 316L powder with 30 µm ± 15 µm particle diameters was used [22]. The vertical stage motion between layers was 50 µm. A 400 W fibre laser and galvanometer scanner were used to melt the powder onto SS304 coupons. Light from the laser was focused to a spot with a Gaussian beam profile and diameter of 50 µm. In all experiments, 5 x 5 mm^2 islands were built in each layer, each island comprising adjacent tracks with alternating laser scan directions. Between layers, the laser scan orientation within the islands was rotated by 90°. The default build conditions were: laser power 200 W, scan speed 0.75 m/s and 110 µm track spacing, with the scan direction parallel to the direction of the cross-flow (peak flow rate 2.1 m/s). Some of these parameters were varied from these default values during the study, as described in the results section.

3. Numerical model

COMSOL multiphysics was used to analyse LPBF cross-flow dynamics including the vapour jet and plume. In our previous work, we used a 2D axisymmetric model, as the focus was only on the atmospheric flow induced by the vapour jet and plume rising rapidly from the melt pool. In order to incorporate the asymmetries introduced by the cross-flow, a 3D version of the model was created for this study. The governing equations used and accompanying literature have been covered in detail in [15], so only an outline of the model will be given here.

The geometry consists of a 350 x 80 x 50 mm^3 block comprising the fluid domain, and a 5 x 10 x 1 mm^3 block comprising the solid domain, as shown in Fig. 2. Symmetry was assumed in xz-plane, which intersects the substrate, vapour jet and cross-flow exactly in the middle. The powder layer was omitted from the model, as the discrete nature of powder particles cannot be captured using FE alone, and previous experimental observations have shown that the laser interacts directly with the melt pool. The fluid domain, which is a mixture of Ar and Fe, was prescribed non-linear properties as presented in [23]. The solid domain was defined as stainless steel using the temperature-dependent properties from Kim [24]. A locally refined tetrahedral mesh was used, as indicated by the colour scheme in Fig. 2. Mesh sizes ranged from ~2 µm, at the location where the laser beam interacts with the substrate, to ~5 mm further downstream of the substrate. Each case had a run time of ~28 hours on a workstation with two Xeon® E5-2697 v4 (2.3 GHz) processors and 256 GB DDR4 RAM.

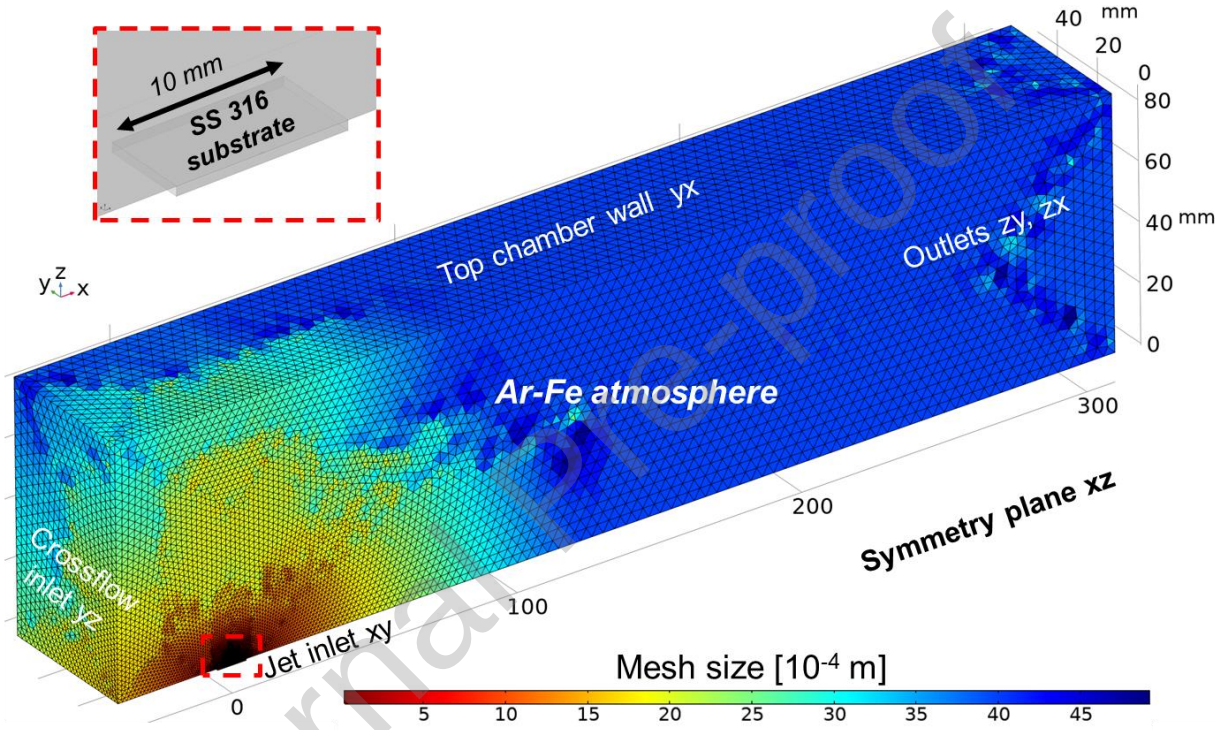

Fig. 2 Geometry, mesh and FE model overview

The Reynolds-averaged, compressible Navier-Stokes (RANS) equations were used to solve for the fluid flow, coupled with a convection-diffusion scheme to track the transport of metal vapour. An energy balance was used to account for the temperature in both domains, given the energy input from the laser. Only steady state solutions were calculated, as they were found to give informative results but with significantly reduced numerical cost.

The metal vapour jet enters the fluid domain at the speed of sound of the gas at the given temperature, which is usually a few hundred degrees above the boiling point. The concentration of metal vapour in the jet is determined by the local vapour pressure, and how far it goes above atmospheric.

The Ar cross-flow enters the domain from the left-hand side, with a profile based on previous simulations of the flow straightener device. To match the measured Ar cross-flow velocities, the peak Reynolds number at the inlet (defined as $Re = \rho U D_H / \mu$ with the hydraulic diameter D_H = 0.01 m equal to the cross-flow device's outlet area divided by its wetted perimeter, and ρ = 1.62 kg/m^3, μ = 23.6 µPa*s [23]) was calculated as 1400 and 850 for high flow and low flow, respectively. The surface roughness of the powder bed was assumed to have a negligible effect on the flow and was not included in the model. The top and bottom parts of the domain are treated as no-slip walls, and the outer boundaries are treated as outlets.

4. Results

In the following subsections, various build process parameters were varied, including the gas flow rate, the orientation of the laser scan with respect to the direction of the cross-flow, and the laser power and scan speed. The figures presented are annotated stills of high-speed videos available online, which the reader is encouraged to watch alongside the text.

4.1 Influence of the cross-flow and powder layer (layer 1)

Initially, a bare coupon was used to provide a baseline comparison of the process without the extra complexity of the powder particles. The 5 x 5 mm^2 island was comprised of 45 tracks, with alternating back and forth scanning, 200 W power, 0.7 m/s scan speed and 110 µm hatch spacing, i.e. the default build conditions. Fig. 3(a), captured during track 2 of the island scan, shows the refractive index gradients associated with the laser plume. Due to the strong energy flux on the steel surface, a vapour micro-jet is ejected vertically, causing strong density gradients within the Ar atmosphere. These are due to the jet's temperature, metal concentration and pressure gradients, stretching ~2 mm vertically from the surface. Beyond that, a trail of fumes and refractive index gradients appear due to the laser's motion during the previous track.

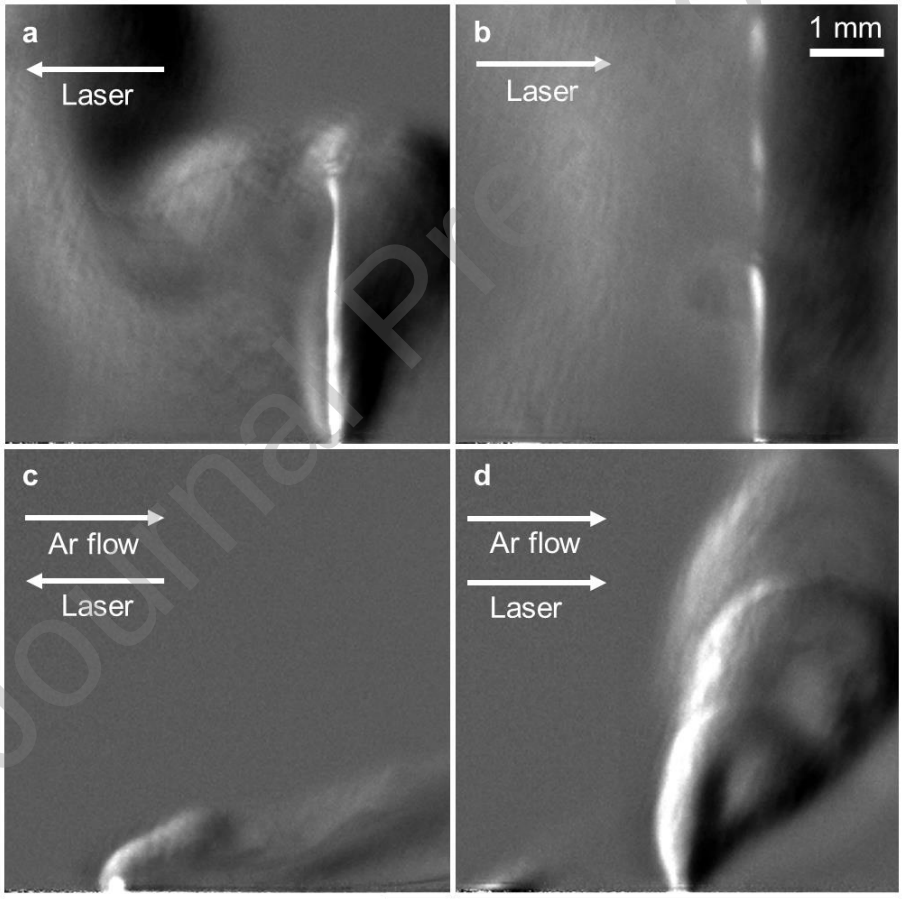

Fig. 3 Schlieren visualisations of the laser plume on the build plate during a 45 track island scan. (Top) Without cross-flow: (a) track 2 and (b) track 45. (Bottom) With cross-flow: (c) track 2, laser scanning in the direction opposite to the flow and (d) track 45, laser scanning in the same direction as the cross-flow.

The jet's vapour condenses to form particulates that undergo various growth processes as they cool [25,26], reaching sizes in the ~100 nm range within the first few mm above the melt pool [10]. For clarity, the difference between solidified *vapour nanoparticles* discussed here, and *metallic powder particles* used for PBF (typically 10 – 100 µm size range) is emphasised. When nanoparticles are mixed with the ambient Ar, they absorb and refract the incident light, changing the complex refractive index of the medium. Macroscopically, in regions where the nanoparticles are in high concentration, they absorb broadband light and thus appear as black fumes following the flow's streamlines. At the edges of the flow, where their concentration tends to zero, they form density/refractive

index gradients that delineate the laser plume seen in the schlieren images. Towards the top of Fig. 3(a) a trail of fumes and refractive index gradients appear due to the plume produced by the previous track.

Without extraction, this aerosol cloud remains over the scanned area, with varying concentrations of nanoparticulates. This effect is demonstrated by the refractive index gradients at the edges of the scanned area in Fig. 3(b), which was captured during the last track of the island scan. The path of the laser beam is visible in certain regions of the plume in both images where it was scattered and absorbed by the aerosol cloud. In the schlieren setup, 99.99% of the 1070 nm radiation was blocked by KG-5 infra-red absorbing glass, suggesting that the white lines in the image are due to radiation emitted by the heated nanoparticles. The relation between an increased concentration of nanoparticles and higher absorption is highlighted by the emitted light as the laser scans through the fume trails.

Clearly, vapour and fumes are transported in the direction of the Ar cross-flow when it is introduced over the bed, Fig. 3(c) and (d). The frames in Fig. 3(c) and (d) were recorded during tracks 2 and 45, respectively, with the laser travelling in different directions with respect to the cross-flow. The homogeneous background in both cases indicates that fume was extracted fully without build-up. The absence of a laser beam outline within the plume structure shows that scattering and absorption is drastically reduced with the cross-flow present. When the laser is travelling counter to the flow direction, Fig. 3(c), the refractive index gradients are almost completely horizontal, while in Fig. 3(d) the plume has a more vertical tilt and reaches higher into the chamber. This difference is simply an effect of the relative velocity between the laser scan and cross-flow in the reference frame of the observer. The accompanying video shows that the plume height for earlier tracks also in the same direction as the cross-flow (tracks 3, 5, etc.) is slightly less than for track 45, due to the build-up of heat during the scan, but this is a second order effect compared to the scan direction. It is interesting to observe that laser beam always passes through a portion of the laser plume, even when the scan direction is towards the cross-flow.

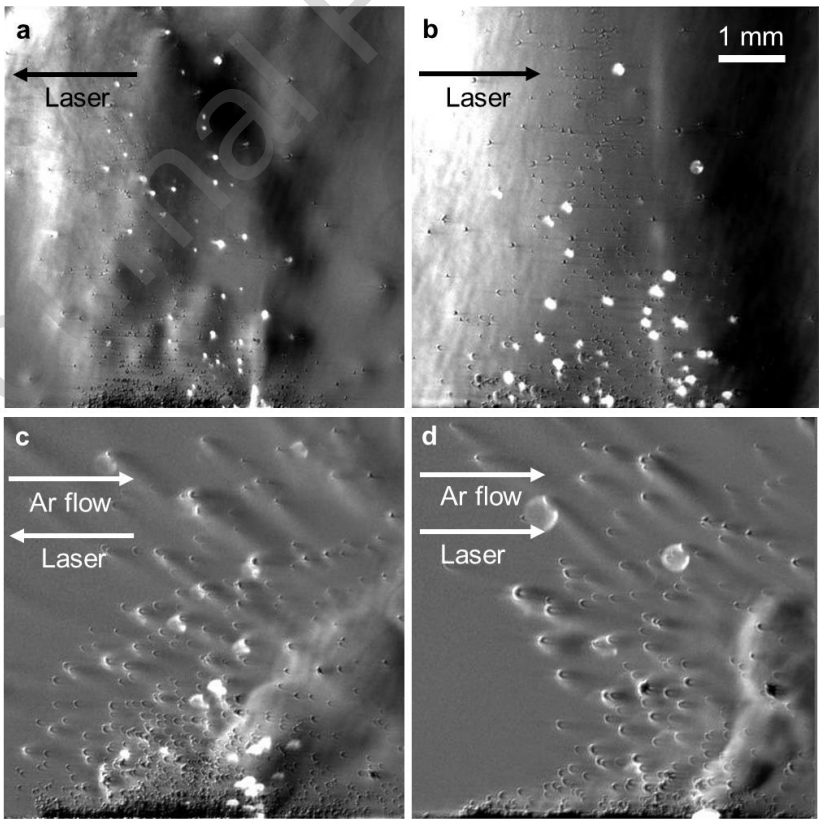

Fig. 4 Schlieren visualisations of atmosphere over powder bed, for powder layer 1. (Top) Without cross-flow: (a) track 2 and (b) track 45. (Bottom) With cross-flow: (c) track 2, laser scanning in the direction opposite to the flow and (d) track 45, laser scanning in the same direction as the cross-flow.

Fig. 4 contrasts operation during an island scan in the first powder layer spread directly on to the build plate. The same (default) conditions were used for direct comparison with Fig. 3: Fig. 4(a) and (b) are without a cross-flow and 4(c) and (d) are with the high cross-flow. These images, and the associated videos in the supplementary material, are the first reported schlieren images recorded with sufficient magnification to resolve individual cold powder particles, as opposed to only the refractive index trail from heated particles. Due to the high optical magnification, the depth of field was relatively short, and therefore an increasing number of particles appear crescent-shaped due to defocus as the island scan progresses away from the focal plane. The direction of the crescent depends on whether a particle was closer or further away from the camera's focal plane. Several islands were scanned on the same coupon, so the amount of defocus in some later figures is more pronounced. In all cases in Fig. 4, a large number of particles become airborne due to the laser scanning. More cold powder particles are lifted during the first track of the island scan, Fig. 4(a) and (c) compared to the later tracks, Fig. 4(b) and (d), due to the increased powder availability from both sides of the laser track in the fresh powder bed. As in the case without powder, significant fume build-up enabled thermal radiation from heated nanoparticles to be observed in the laser path without the cross-flow, Fig. 4(a) and (b), but was not present with the cross-flow, Fig 4(c) and (d).

A variety of interactions between the laser, airborne powder particles and the vapour jet can be observed, which complement those of recent imaging experiments [27–29,15,13,30]. Particles become entrained in the atmospheric flow induced by the vapour jet, with those reaching the proximity of the jet being ejected. The direction depends on process settings and the resulting melt pool morphology; particles are predominantly ejected upwards here. The trajectory of some of the entrained particles intersects that of the laser beam and vapour jet: energy is transferred and particles that have been heated sufficiently emit thermal radiation. It is evident from Fig. 4 that these hot particles from close to the melt pool and laser beam are generally ejected with the greatest speed and therefore rise higher above the powder bed. In contrast, cold entrained particles move slower and remain closer to bed. Without the cross-flow, Fig. 4(a) and (b), the primary source of momentum change acting on the airborne particles is the vapour jet. Therefore, during the second and subsequent tracks, the laser plume drags cold particles higher, resulting in a chaotic mixture of hot and cold particles high above the powder bed. When the cross-flow is on, however, cold particles that are within the cross-flow stream do not remain in place long enough for the laser to interact with them several times, reducing the number of interactions and hence the height of cold particles above the bed, Fig. 4(c) and (d).

Clusters of powder particles that have been partially sintered to form agglomerates on the powder bed are also entrained, particularly from the second track onwards. Further interaction between such agglomerates and the laser causes them to fuse together completely, forming spherical particles of diameters greater than ~100 μm [13,30]. Occasionally, a direct interaction between airborne particles and the laser beam forms a vapour jet on the particle's surface that imparts downwards momentum onto the particle and changing its trajectory back onto the powder bed, potentially disturbing the powder bed. The interaction of the laser with particles and agglomerates produces more fumes than with the substrate alone, as evidenced by the strong refractive index gradient built-up over the processing area in Fig. 4(a) and (b), which despite identical laser processing parameters is more pronounced compared to the case without powder, Fig. 3(a) and (b).

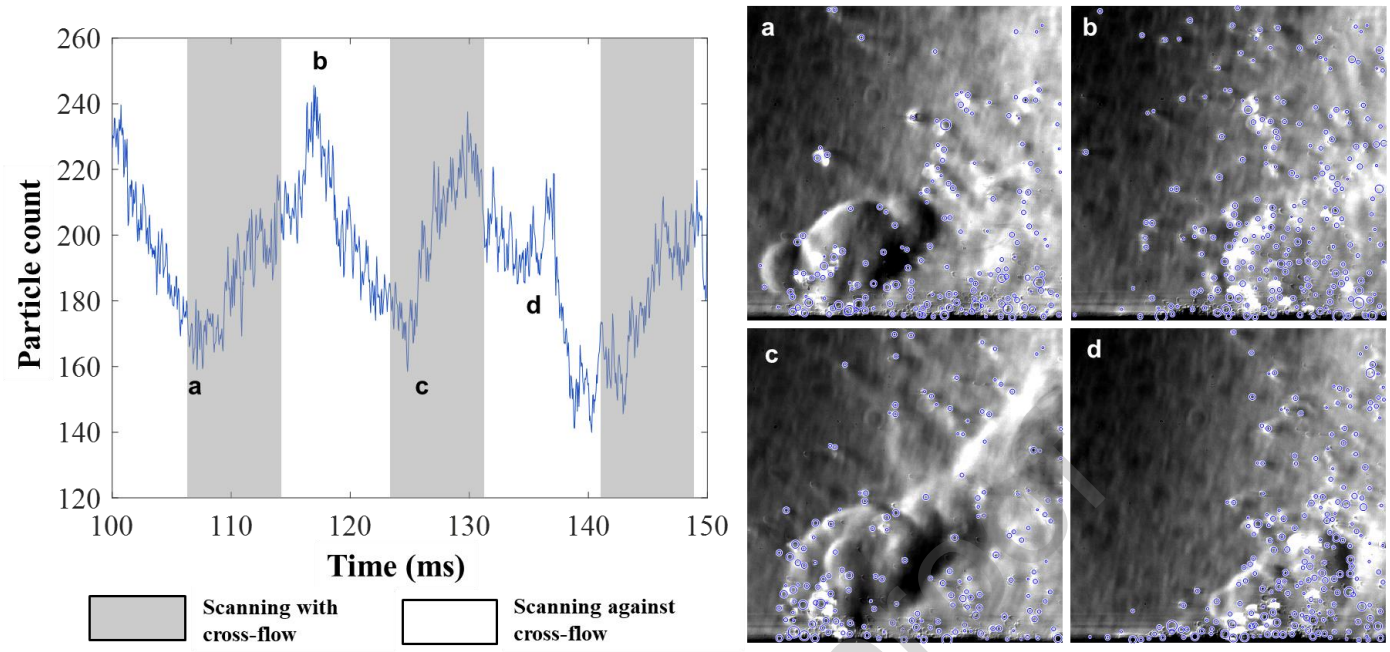

Fig. 5 (Left) Airborne particle count over ~1000 frames during the island scan of powder layer 1. The grey-shaded areas of the graph represent periods when laser scan was in the same direction as the Ar flow. (Right) Frames (a-d) show individual frames corresponding to the local minima and maxima in the graph.

The total number of airborne particles for every frame in the image sequence represented in Fig. 4(c) and (d) was estimated using image processing. A circular Hough transform [31] was found to consistently detect over 85% of particles with minimal false positives. Removal of the background refractive index fluctuations with the tare image, as used in Fig. 4, reduced the accuracy of the Hough transform: hence the 'raw' images were used for particle identification. A plot of the total particle count over a period of ~50 ms is shown in Fig. 5. The transient dynamics of powder motion result in local maxima and minima in the number or airborne particles, which are related to the change in laser scanning direction indicated by the grey-shaded areas of the graph. During the beginning of a track in which the laser scan is in the same direction as the Ar flow, particles become airborne and the particle count starts to increase, Fig. 5(a). The particle count continues to increase until approximately half-way into the following track, with the laser now scanning opposite to the flow, Fig. 5(b). At that point, particles that were ejected during the previous track and the beginning of the current track have been removed by the cross-flow and are no longer over the island. The count decreases until the particles start being ejected from the next track, Fig. 5(c). Overall, a rising-and-falling trend is observed in the particle count, due to the alternating laser scan pattern. Collisions between particles already within the cross-flow stream and particles freshly ejected from the bed can cause a larger number of particles to remain within the field of view as in Fig. 5 (d). Following the collision, their velocities homogenised, and they were extracted as a group leading to the minimum at t = 140 ms. Such stochastic events occur repeatedly during a build, interlinked with the denudation of the powder bed, laser-particle interactions and redeposition of powder.

4.2 Influence of cross-flow velocity under steady-state build conditions (layer 30)

To understand how the crossflow affects the process when a steady layer thickness has been reached, cubes were manufactured comprising multiple islands with a 90° rotation in the laser scan orientation between layers. A contour scan marking the perimeter of the scan area was included at the beginning of each layer. Builds were undertaken at both the high and low cross-flow settings. The imaging was carried out at layer 30, with the laser scan orientation still parallel to the Ar cross-flow. A small pile of powder builds up at the front and back of the powder bed during the spreading of multiple layers. This pile of powder falls within the line of sight of the schlieren

instrument, forming a small region across bottom of each image in which the base of the laser plume was obscured. Additionally, under high flow, a few loose powder particles from the pile were carried by the stream and are visible in the background of the corresponding videos, from which the frames for Fig. 6 were taken.

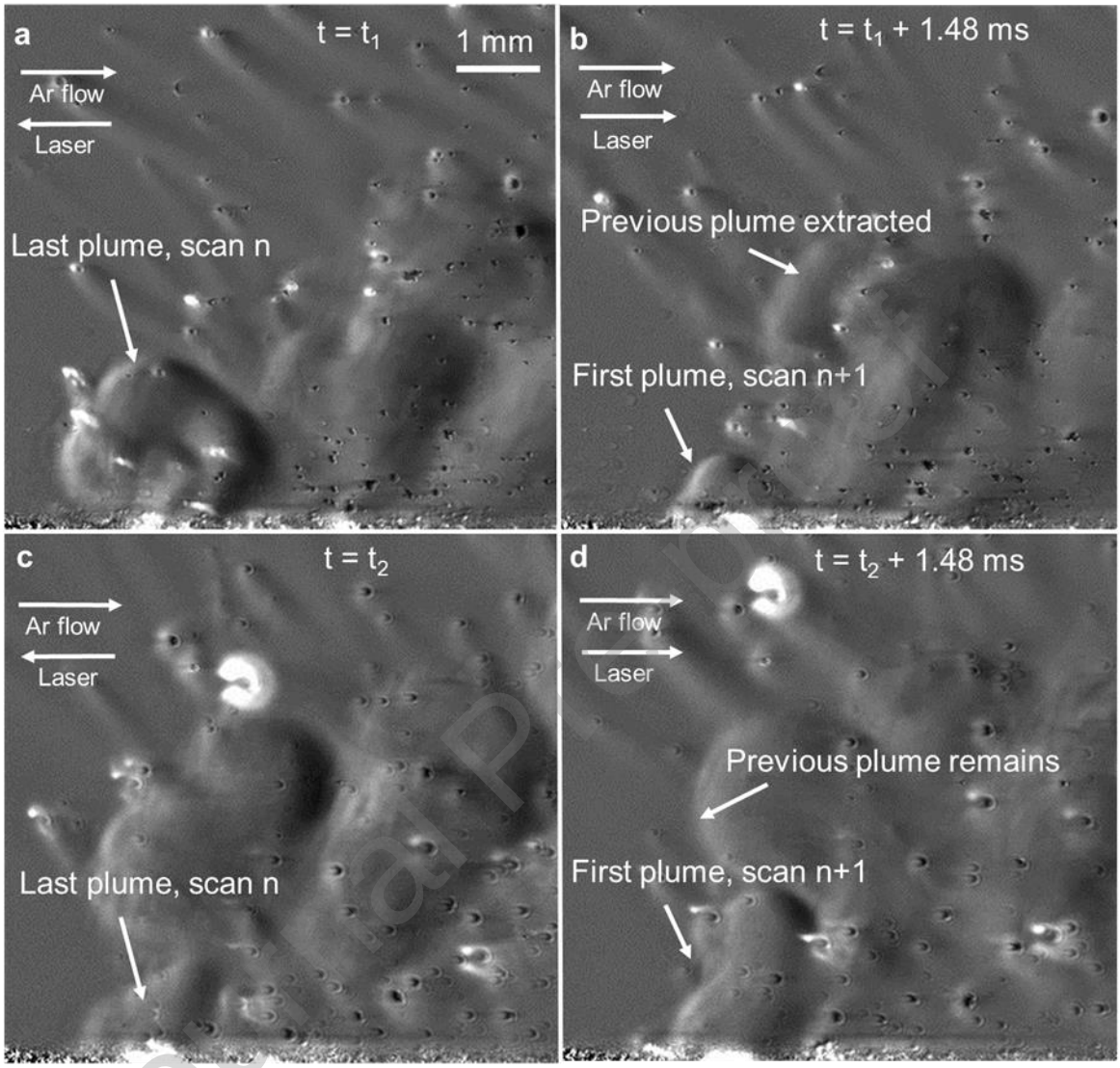

Fig. 6 Schlieren imaging of by-product extraction for layer 30: (Top) (a) and (b) high flow condition; (Bottom) (c) and (d) low flow condition. The first image for each condition (a) and (c) shows the end of one track; the second image (b) and (d) show the start of the subsequent track.

In Fig. 6, frames (a)-(b) and (c)-(d) were captured while using a high and low flow respectively. The videos in the accompanying material, show that the process at layer 30 is less dynamic compared to layer 1, previously seen in Fig. 4, possibly because the particles are packed more stably due to the increased thickness of the powder layer and the surface texture of the preceding layer [16]. Frames (a) and (c) were captured at the end of a track, showing the last set of refractive index gradients for that track. Frames (b) and (d) were captured 1.48 ms (32 frames) later, just after the beginning of the next track. Both images (b) and (d) show formation of the initial plume for this next track close to the vapour jet, which is similar under both flowrates. However, the position of the plume from the end of the preceding track is different between the two cases. For the high cross-flow, Fig 6(b), the plume from the preceding track was removed by the cross-flow from the path of the laser beam. For the low cross-flow, Fig 6(d), the extraction rate is smaller and therefore fumes remain within the scanned area longer. The video footage reveals that the beam passed through the fumes much more frequently under low flow conditions and especially during the start of each track, as the by-products of the previous track hadn't yet cleared. The laser beam's path through the atmosphere is occasionally visible under low flow, highlighting the effect of the lower extraction rate.

The number of ejected particles during the scanning of each 5 x 5 mm^2 island was estimated using the circular Hough transform, Fig. 7. At the onset of the scan, a large number of particles are ejected due to the initial contour scan. After t ~ 80 ms, the normal back and forth scanning commences. For both cases, the particle count varies significantly during the scanning, due to the various stochastic events discussed previously. However, a lower number of particles is observed consistently throughout the island when using the high flow. With a lower number of particles above the processing area, collisions between particles and laser-particle interactions become less frequent.

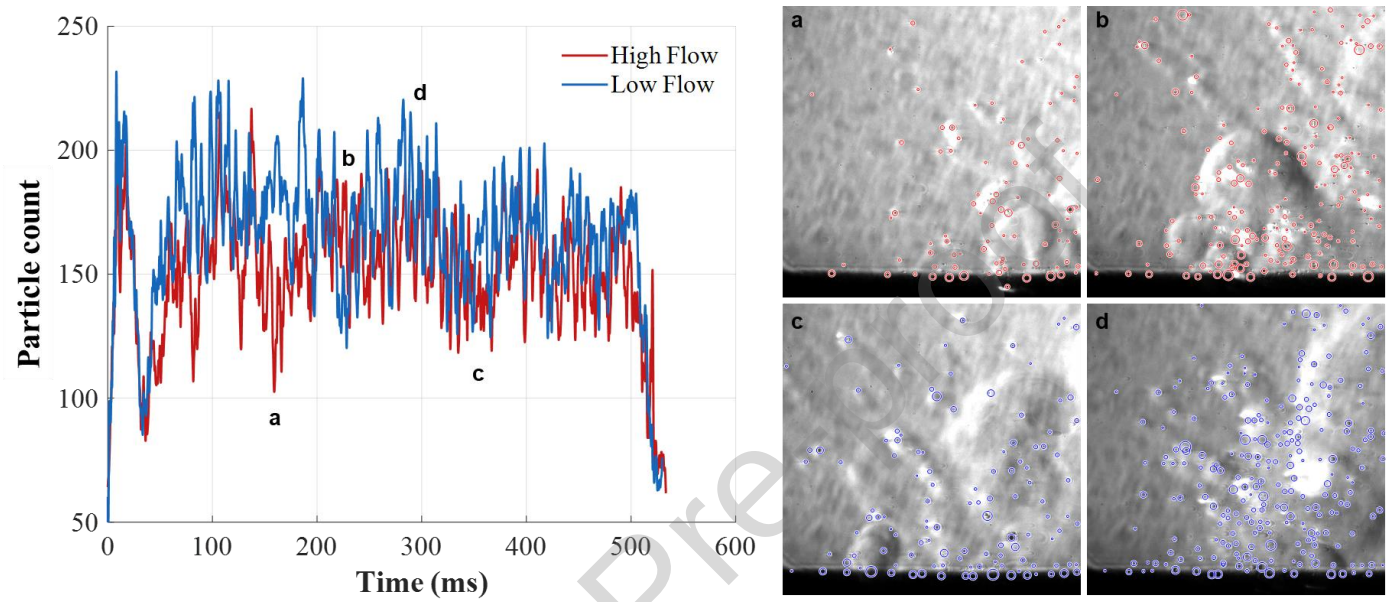

Fig. 7 Graph: Total number of airborne particles during island scan, for layer 30. Images: (Top) (a) and (b) High cross-flow; (Bottom) (c) and (d) Low cross-flow. Typical frames when the count reaches (a), (c) local minima and (b), (d) local maxima are shown for each flowrate.

The data from the direct imaging complement these observations from the schlieren imaging. Fig. 8(a) and (b) show raw images of the top view of the island scan for layer 30 under the same conditions of high and low cross-flow, respectively. The videos in the accompanying material, from which these frames were taken, show disturbances to the powder bed where ejected spatter, particles and powder agglomerates land. Dark condensate is visible in the plume above the powder bed, as well as local distortions (translations) of the image of the powder bed due to the refractive index variations in the laser plume. To enhance the visibility of these features, the background of every frame was removed through division by a tare image (the first frame in the sequence) followed by contrast stretching, the same as the background removal employed with the schlieren images. Fig. 8(c) and (d) show the background removal applied to images (a) and (b), in which impact disturbances in the powder bed and the dark condensate above the powder bed are more clearly visible. This processing results in a background-oriented schlieren effect [32] in which refractive index gradients distort (translate) each image with respect to the initial background image. The effect of the laser plume's propagation over the powder bed is therefore visualised in this manner.

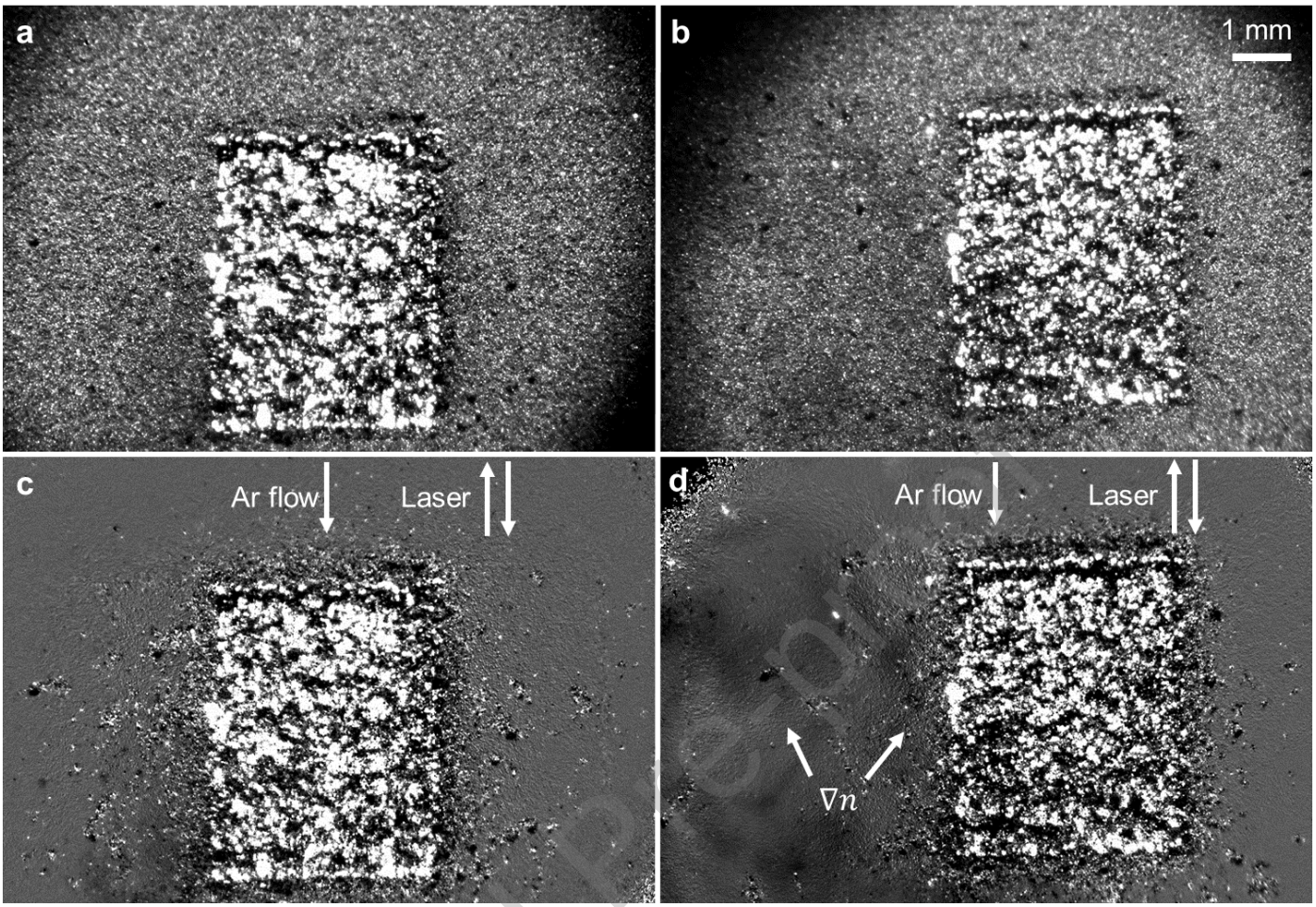

Fig. 8 Direct imaging during processing of layer 30, with the laser scan orientation coincident with the cross-flow. (a) High cross-flow and (b) low cross-flow conditions. The corresponding images with background removal (background oriented schlieren) are shown in (c) and (d).

Fig. 8 shows that for both the high and low cross-flow cases, there was no significant vapour cloud build-up over the finished tracks and that the by-products were extracted. However, the refractive index variations are significantly stronger in the low flow case. The schlieren images in Fig. 6 showed that the laser plume rises higher above the bed with the low flow. Hence, the stronger refractive index variation in the low flow case observed in Fig 8(d) is not just due to the slower rate of extraction: the increased height of plume above the bed means that the effect of a given refractive index gradient has an increased effect on the image distortion.

Fig. 9 shows the results from the finite element model with the default process conditions and the magnitude of the input cross-flow set to match the low and high cross-flow experiments. Flow velocity (left) and temperature (right) fields are plotted over the xz-planar section of the 3D domain at the middle of the plume. Due to the large difference of values between the hundreds of m/s in the vapour jet and a few m/s of the cross-flow, the common logarithmic scale between 10^{-2} and 10^{2} m/s was used for plotting the velocity. The range of the temperature plot is chosen to emphasize how much of the region is at ambient temperature. The same linear arrow plot is interposed on both the fluid velocity and temperature coloured surfaces, scaled in length and grayscale to show the fluid velocity magnitude but capped to 2 m/s to show the profile of the cross-flow.

At both cross-flow rates, the plume acts as a barrier to the cross-flow, with the high upwards momentum imparted by the vapour jet countering the sideways momentum of the cross-flow. The model is in good agreement with the experimental results: the momentum in the high cross-flow is enough to fully incorporate the upwards plume, Fig. 9(c), whereas the momentum imparted onto the plume at the low cross-flow is not sufficient for it to be fully incorporated in the stream, Fig. 9(a), and it is deflected diagonally upwards. A low velocity zone is generated directly behind the plume in both cases, similar to the classic flow around a cylinder. For both flowrates, the high

temperature zone is restricted close to the substrate: only a few mm above the jet's origin the temperature returns to ambient due to the rapid convective cooling of the cross-flow and the rapid heat transfer from the plume to its surroundings. Hence the refractive index variations away from the vapour jet in Figs 6 and 8 were not due to temperature gradients in the laser plume.

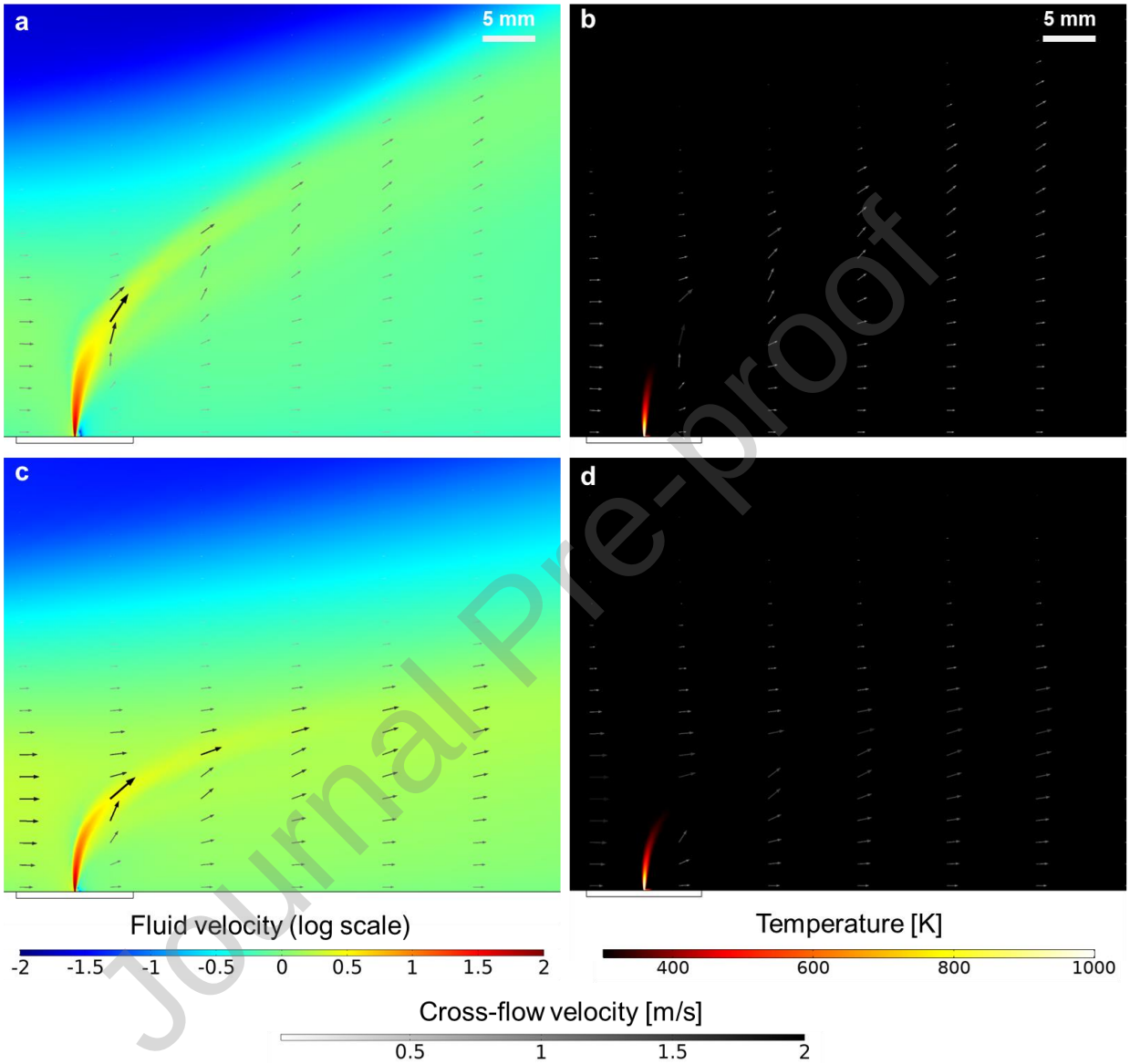

Fig. 9 (a) and (c) Calculated velocity and (b) and (d) temperature distributions for the symmetry plane, midway through the plume. (Top) (a) and (b) Low cross-flow; (Bottom) (c) and (d) High cross-flow conditions. A linear arrow plot showing the flow velocity capped to 2 m/s is overlayed in all plots.

The steady-state nature of the model means it cannot be used to corroborate the rate of vapour/fume extraction observations from the high-speed footage. Instead, the model can predict the spatial distribution of the vapour over time, complementing the transient information of the imaging. The effectiveness of extraction can be visualised in terms of Fe content in the atmosphere, as shown in Fig. 10. Fig. 10(a) and (b) again show the flow velocity calculated from the finite element model with the default process conditions on the xz-plane section of the 3D domain at the middle of the plume, but for the full extent of the fluid domain shown in Fig. 2. The corresponding Fe concentration over the same region is indicated in Fig. 10(c) and (d) for the low and high cross-flow rates, respectively, and clearly extends significantly behind the plume in contrast to the temperature distribution seen in Fig. 9. Hence, the refractive index gradients seen in Fig. 8 that extend several mm from the melt pool can be attributed predominantly to metal concentration gradients in the plume.

Close to the laser spot, the Fe concentration is 100%, due to the strong evaporation from the surface. The vapour jet cools as it is transported upwards, with the concentration dropping to around 10^4 ppm within the first few mm, before dispersing into the cross-flow. When the total momentum in the plume is not fully counteracted by that of the cross-flow, Fig. 10(a) and (c), Fe species exit the cross-flow stream with an upwards trajectory. As a result, an appreciable portion of the evaporated Fe ends up recirculating or condensing on the upper surfaces of the LPBF chamber. As the momentum in the stream is increased, Fig. 10 (b) and (d), the plume is dispersed faster and fully extracted within the height of the outlet. The smaller size of the plume in the high flow case highlights that when species transport is dominated by convection rather than diffusion, more efficient dispersion of the aerosol cloud is achieved.

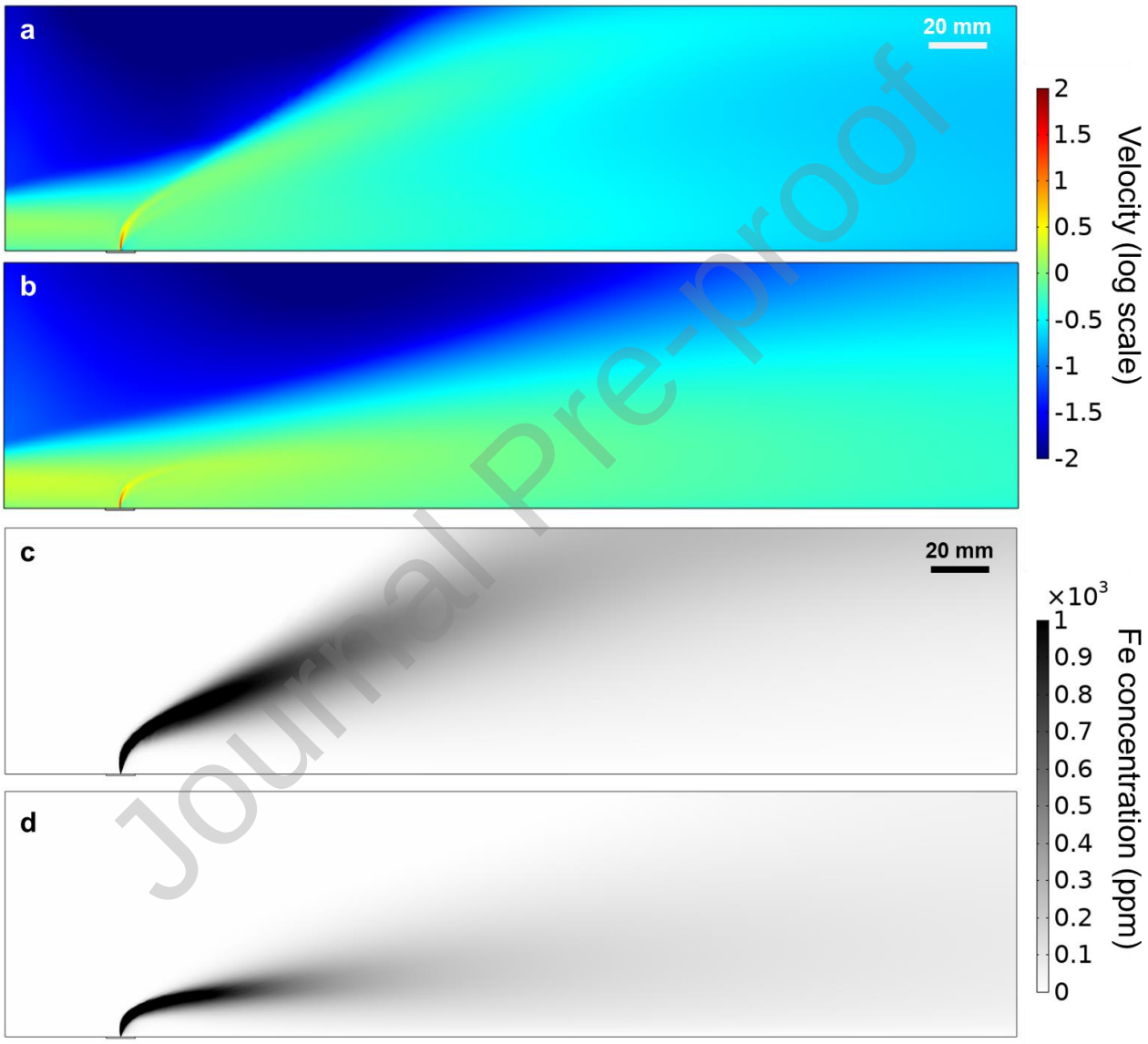

Fig. 10 Calculated velocity plots: (a) High flow; (b) Low flow. Fe concentration plots: (c) High flow; (d) Low flow. If the cross-flow stream is insufficient to incorporate the plume, fumes are ejected with an upwards trajectory and stagnate on the upper walls of the chamber.

4.3 Influence of laser scanning orientation

Varying the orientation of the laser scan between islands and layers is an essential part of the LPBF process because the temperature gradients experienced by the part vary greatly with the direction of scanning and mass is consolidated unevenly within any one island. However, the direction of the crossflow always remains the same, resulting in a variation between layers. To complement the above experiments where the cross-flow was parallel to

the laser scan orientation within the island, imaging was also carried out for laser scans perpendicular to the cross-flow. In this case, the starting point of the laser tracks in the island plays an important role, because they can either advance towards the inlet or towards the outlet. While both scenarios occur during layer rotation, more adverse conditions are expected when the laser plume and powder particles are pushed by the Ar flow towards the region of the island that remains to be processed. Hence imaging was carried out with adjacent laser scan tracks in the island advancing towards the cross-flow outlet.

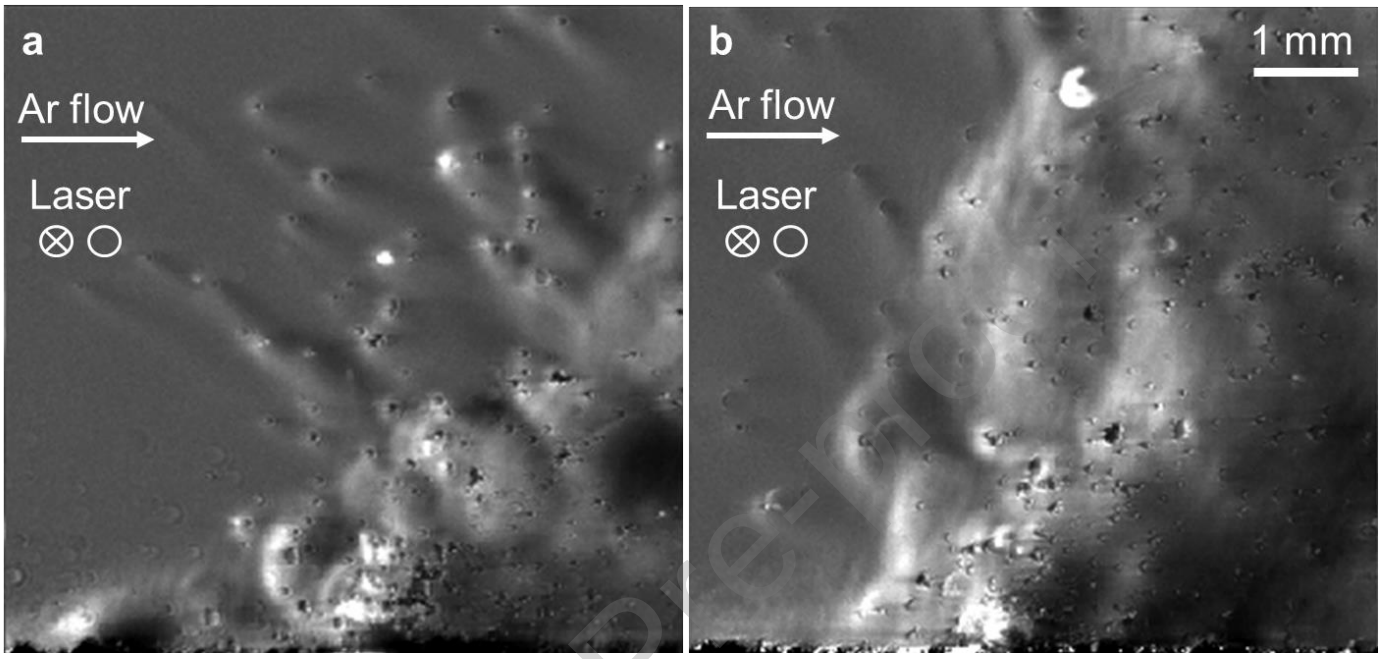

Fig. 11 Schlieren imaging during processing of layer 35, with cross-flow perpendicular to the laser scan direction, under (a) high flow and (b) low flow.

Fig. 11(a) and (b) show frames from schlieren imaging in the high and low flow conditions respectively, with the laser scan orientation perpendicular to the cross-flow. Due to the accumulation of vapour along the scan direction, which now coincides with the line-of-sight of the schlieren instrument, the refractive index gradients over the scanned tracks are stronger than in Fig. 6. Fig. 12(a) and (b) show frames from the corresponding direct imaging for the high and low cross-flows, respectively, with Figs. 12(c) and (d) showing the background removal described previously. Similarities with the parallel scanning cases are observed, with refractive index gradients extending higher above the powder bed, Fig. 11(b), and covering a greater area, Fig. 12(d), for the low cross-flow extraction rate.

A difference was observed in the behaviour of the cold powder particles and powder agglomerates that become airborne. In the previous case when the scan orientation was parallel to the cross-flow, Fig. 6, these particles were dragged parallel to the laser tracks and were available in both laser scan directions, and at both high and low cross-flow, for the stochastic interactions described previously. However, when the laser scan direction is perpendicular to the flow, the high cross-flow in Figs. 11(a) and 12(c) exerted sufficient drag on the airborne particles to remove them from the processing region and prevented them from interacting with the melt pool and laser. As a result, the sintering of loose particles is not promoted, and the few agglomerates that are formed do not generally reach the melt pool. In contrast, at the low cross-flow rate, Figs. 11(b) and 12(d), the local flow around the vapour jet was sufficient to drag a significant number of the airborne particles back towards the melt pool *against* the direction of the cross-flow. The airborne powder remains for longer in the vicinity of the melt pool and laser path, which promotes the formation of agglomerates and their inclusion back into the build. The movement of the airborne particles against the cross-flow at low cross-flow speed, and their increased interaction with the laser, is most easily seen in the in the videos corresponding to Figs. 11(b) and 12(d) in the accompanying material. The increased number of agglomerates at low cross-flow compared to high cross-flow is seen in the ejecta on the

powder bed; the less homogeneous texture of the scanned island at low cross-flow shows that many of these agglomerates were incorporated back into the melted tracks. Indeed, the smoother surface texture of the island formed when scanning perpendicularly to the high Ar cross-flow, compared to that in Fig. 8(c) for the parallel scan, indicates that it is a more favourable build condition.

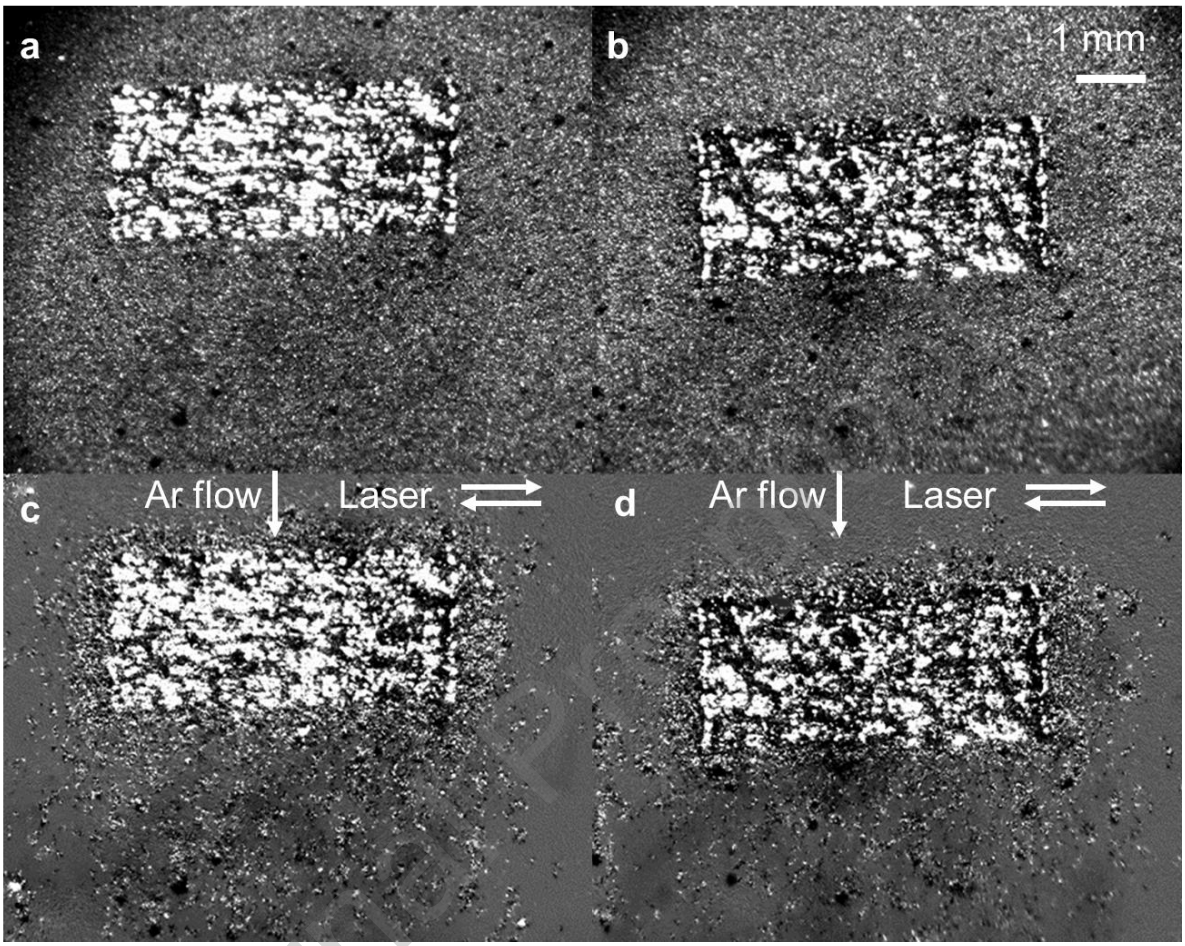

Fig. 12 Direct imaging during processing of layer 35 with the laser scan orientation perpendicular to the cross-flow. (a) High cross-flow and (b) low cross-flow conditions. The correcsponding images with background removal (background oriented schlieren) are shown in (c) and (d).

4.4 Influence of laser energy density

The incident laser flux on the powder bed determines the intensity of evaporation by modifying the surface temperature [13,15,33]. Controlling the scanning speed changes how the heat is distributed over time, which also changes the surface temperature. To understand how the extraction process is affected by this, the experiments were repeated using 100 W power and 0.4 m/s scan speed, chosen for a comparable line energy to the default setting of 200 W, 0.75 m/s used previously.

By comparison with the higher laser power dataset, Fig. 6(a), the schlieren image of Fig. 13(a) shows that lower laser intensity generates less vapour and fumes. Consequently, the schlieren gradients in the plume were less pronounced and with fewer oscillations, possibly due to a less dynamic melt pool. The cross-flow and plume are much larger scale than the vapour jet, and so any change to the melt pool shape at the lower power only has a limited effect on the measured plume. Fewer airborne powder particles were observed with this parameter set, as the slower vapour jet induces a weaker atmospheric flow and thus exerts weaker upwards drag forces. Only particles that come close to the melt pool accumulate enough momentum to become airborne. Such particles tend to fuse together due to the heat in that area, which explains the larger size distribution amongst airborne particles compared to the high-powered case. Additionally, the weaker drag forces combined with the reduced scan speed of the laser increases the occurrence of powder agglomerates in the vicinity of the melt pool.

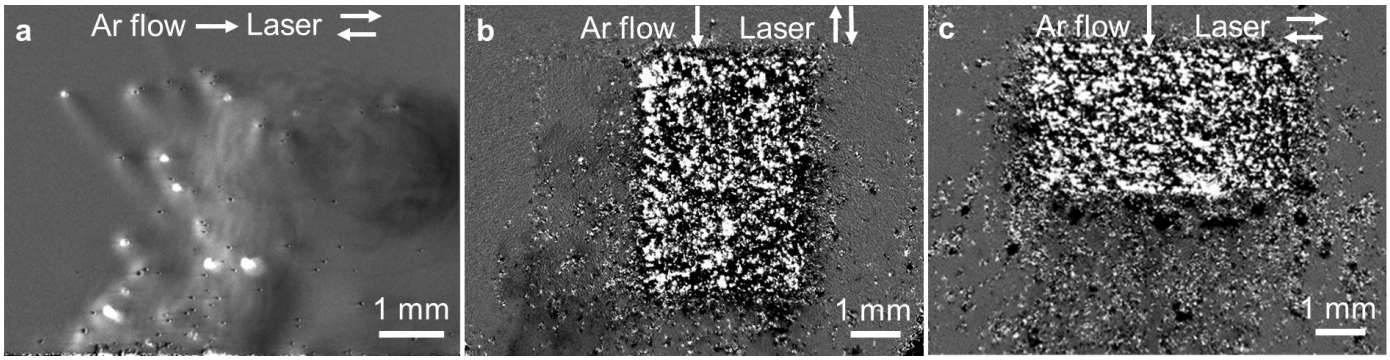

Fig. 13 Low laser power and scan speed. (a) Schlieren imaging and (b) direct imaging during layer 30. Direct imaging during layer 35.

The top view showed a similar surface roughness for both the parallel and perpendicular scan directions, Figs. 13 (b) and (c). No improvement was seen with the perpendicular scan at this lower power and scan speed, due to the reduced number of loose powder particles and the increased number of powder agglomerates. Indeed, a rougher island was manufactured for both scan directions with the low power set compared to the standard parameters, Fig. 8(c). While surface roughness is dependent on several factors which change with laser parameters, such as the solidification dynamics in the melt pool and the degree of overlap between consecutive weld beads, these results show that the sintering and inclusion of powder agglomerates also has a marked effect.

5. Discussion

The laser plume is a complex structure, which is driven by the strong convection of the metallic vapour jet. The peak velocity of this jet is mainly dependent on the surface temperature, density of evaporated species and ambient pressure, with a narrow Knudsen layer forming directly over the evaporating surface [34]. In the simplified model presented, by assuming that the fully-developed steady flow from that surface is choked and the Mach number cannot be higher than 1, the upper limit of the velocity is the local speed of sound

$$u = \sqrt{\frac{\gamma k_B T}{m}}$$

where γ is the adiabatic index, k_B is Boltzmann's constant, T the temperature and m the atomic mass of the evaporating species. The laser power absorption in the heat transfer equations used in our model was tuned so that the surface temperature peaked at around ~3,400 K (implying that a small degree of superheating occurs), resulting in a peak velocity of ~900 m/s, over a ~40 µm diameter area. Despite the simplifications of this approach, recently presented self-consistent numerical modelling [35] that included the full melt pool dynamics and a more detailed treatment of the inlet pressure, calculated a peak velocity of the same order of magnitude.

The modelling results in Figs. 9 and 10 demonstrated how this energy due to the jet is transported in the Ar atmosphere and under the influence of the cross-flow. In contrast, Fig. 14 shows a much closer view of the laser plume for the high flow condition. Despite the large peak velocity of the vapour jet, the region where the velocity is greater than 100 m/s does not exceed 0.5 mm, Fig. 14(a). The momentum within the first ~3 mm is so high that the jet is unaffected by the Ar cross-flow, regardless of flowrate. Similarly, for the temperature distribution, a length of roughly 1 mm rises above 1,000 K, with only the first ~200 µm being above the melting point. This high-temperature region is sufficiently hot to suggest that airborne powder particles could also sinter or fuse into larger particles by an interaction with the vapour jet, although less frequently than on the powder bed due to the lower number of powder particles in close proximity. In addition to transferring heat, the vapour flux could also impinge on airborne particles interacting with the jet, condensing on the particles' surface. Such events could result in nucleation sites for the growth of oxides on particle surfaces, as measured in [36]. Fig. 14(b) emphasises the observation from Fig. 9 that the temperature distribution in the plume returns to ambient within ~1 mm lateral distance from the melt pool.

Therefore, it is primarily the metal concentration that is responsible for the refractive index variations observed through the plume several millimetres away from the melt pool, Fig. 14(c). It should be noted that the calculated Fe concentrations near the melt pool are higher than we reported in [15], due to an expanded computational volume and stricter convergence criteria.

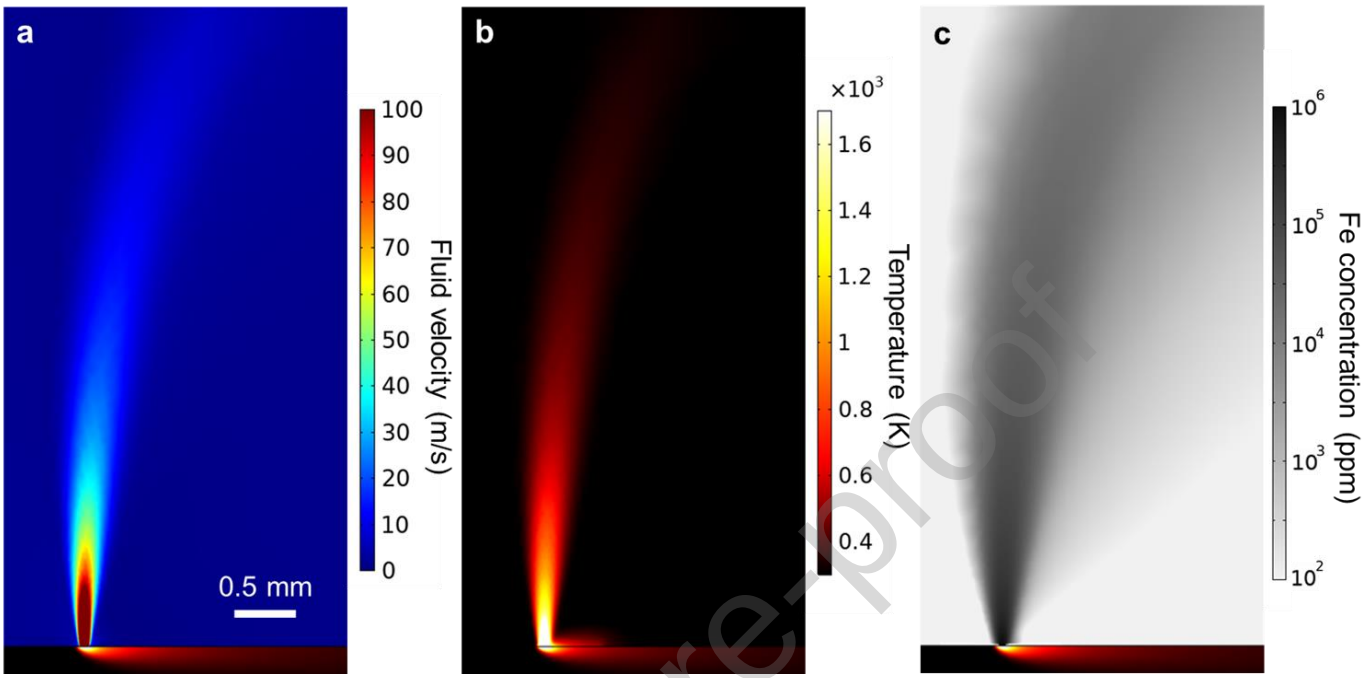

Fig. 14 Calculated velocity (a), temperature (b) and Fe concentration (c), under high flow conditions. The vapour jet is unaffected by the cross-flow close to the laser-material interaction area.

Non-dimensional numbers derived from the model over the length-scales of the vapour jet and initial plume can also help characterise this region close to the melt pool. The Prandtl and Schmidt numbers, defined as $\mathrm{Pr} = \upsilon/\alpha$ and $\mathrm{Sc} = \upsilon/\mathrm{D}$, where υ is the kinematic viscosity, α the thermal diffusivity and D the molecular diffusivity, were calculated for the first 5 mm along the vapour jet's centreline. They were found to be in the range of $0.6 \leq \mathrm{Pr} \leq 1.2$ and $0.4 \leq \mathrm{Sc} \leq 2.2$, showing that momentum, heat and Fe mass dissipate through the Ar atmosphere at similar rates. The flow is being driven by the momentum of the jet, but due to the temperature and concentration gradients, buoyancy forces are present. The relative effect of buoyancy versus flow shear is given by the Richardson number, generally defined as:

$$Ri = \frac{g}{\rho}\frac{\partial\rho/\partial z}{(\partial u/\partial z)^2}$$

where g is the constant of gravity, ρ the local density and u the local normalised velocity. It was found to grow logarithmically in the range $10^{-8} \leq Ri \leq 10^{-4}$ along the first 5 mm of the vapour jet's centreline. Despite an increase of 4 orders of magnitude, the Richardson number was much lower than unity. Therefore, even in a fully developed plume, buoyancy effects are much less significant compared to inertial effects, largely due to the momentum continuously imparted to the fluid by the evaporating surface. The Reynolds number at the jet's core was $Re \sim 300$, mainly due to its small hydraulic diameter (taken as $D_H = D4\sigma_{laser}$), as well as the low density and high viscosity corresponding to the local high temperature and Fe concentration fields.

While it was shown that the cross-flow has a minimal effect on the high-speed vapour jet, once the jet diffuses over ~3 mm and becomes the slower moving laser plume, the cross-flow takes effect. Fig. 10 showed that in the low cross-flow condition, the plume exits the cross-flow stream with enough upwards momentum to reach the top of the build chamber. It can be assumed that the resulting refractive index gradients along the beam's path would defocus it, creating larger variability in the deposited power and thus, a more unstable melt pool. Conversely, under a high flow condition, there was sufficient momentum to fully extract the plume. This was consistent with the visualisations of the corresponding cases. During the experiments, condensate accumulation on the chamber's

upper wall was observed when the cross-flow was at low settings. With the higher velocity, fumes were completely extracted through the outlet. These findings are consistent with those of Reijonen et al. [8], which showed that melt pool dimensions and build porosity were reduced under low flow conditions, but remained relatively constant beyond a certain threshold in cross-flow velocity. The path of the laser beam due to thermal radiation from metal condensate was constantly observable with the cross-flow switched off, Figs. 3(b) and 4(b), occasionally so with the low flow on (at the start of some tracks), while never visible with the high flow. The laser beam path can sometimes be observed in the atmosphere well-above the powder bed in commercial PBF systems, implying that the extraction of metal condensate is incomplete and has accumulated in the chamber.

The small extent of the high-temperature zone of the plume downstream from the melt pool is a key finding of this work. Figs, 9, 10 and 14 show that significant temperature gradients only occur close to the processing area, while appreciable Fe concentrations were predicted to occur hundreds of mm away from the laser. Hence the main contribution to the refractive index gradients (and corresponding density gradients) imaged with the schlieren system on the atmosphere over the powder bed was due to concentration gradients, rather than temperature or pressure gradients. The laser plume rises higher above the powder bed with a low cross-flow, which increases the distortion observed for a given refractive index gradient when looking down through the plume at the powder bed. The transport of metallic vapour, and subsequently fumes, constitutes the main source of interference with light propagating in processing chambers. Thus, even if fumes are extracted from the vicinity of the area being scanned, the diffuse fume trail leading to the outlet has the potential to interfere with light sources. This is an important consideration for in-situ imaging and/or monitoring systems, where aberrations in the atmosphere could result in inaccurate measurements. It is also important for planning layer scan strategies: refractive index gradients in the plume can defocus and translate the incident beam, creating larger variability in the deposited power and a more unstable melt pool. It becomes even more important for the simultaneous operation of multiple lasers where the trail of fumes within the cross-flow stream generated by each laser should be taken into account to ensure that each laser processes through a clean atmosphere. Also, the plume appears as a barrier to the flow locally, as shown in Fig. 9 and Fig. 10. The flow separation around a vapour jet creates turbulent streams over its sides, which could be a consideration for multiple laser operation in close proximity. Finally, calculations or measurements of light propagation in aerosols within LPBF chambers could assume an isothermal medium without accruing large errors.

6. Conclusions

High-magnification schlieren imaging enabled the visualisation of the interactions between the cross-flow, laser plume and individual powder particles in LPBF. The dynamics of these interactions are extremely complex, which when combined with the range of process settings (e.g. laser power, scan speed and direction with respect to the cross-flow), means that there is no simple ‘best solution’ to the cross-flow choice. However, the results reported here provide new insights into the process and hence guidance on practical implementation and on potential future improvements for the laser PBF process.

Vapour from the melt pool condenses forming metallic nanoparticles, capable of interfering with the laser beam. Imaging showed that when the cross-flow velocity was low, scanning through the vapour cloud of previous tracks led to interference with the laser beam. Numerical results showed that if the cross-flow stream carries insufficient momentum, the plume is not incorporated fully, resulting in condensate accumulation within the atmosphere and on the chamber walls. Therefore, radiation tracing the path of the laser beam, sometimes observed in commercial PBF chambers, indicates that metal condensate is accumulating in the chamber and that the extraction is not optimised.

Regular laser scanning of islands resulted in large numbers of airborne particles, due to drag and lift forces exerted by the moving vapour jet. Stochastic interactions between the laser and lifted particles result in disruptions to the process, which deteriorate the build quality. It was shown that a high cross-flow velocity results in fewer particles over the processing area, and therefore fewer instances of deleterious laser-particle interactions.

Generally, the imaging showed that the extraction rate of process by-products is a limiting factor in how fast processing can occur. Adjusting the dwell time between laser scans could allow more time for by-products to clear, possibly improving extraction in older LPBF chambers with limited flowrates.

The angle between the flow and the direction of scanning had a marked effect on the process. Particles pushed in the direction of scanning were more likely to be incorporated in the build at a later scan, deteriorating built quality. A better surface finish was achieved when the cross-flow angle was perpendicular to the scan direction, as particles were dragged away from the scanning path altogether. Conversely, when the cross-flow was parallel to the laser scanning, it was found that more airborne particles were pushed along the laser's path, increasing the likelihood of laser-particle interactions. Consequently, tuning interlayer rotation so that scanning parallel to the cross-flow is avoided entirely could reduce the frequency of defects resulting from such interactions, improving process repeatability.

The momentum in the vapour jet and the rate of fume production were shown to increase with laser power. Additionally, the height of the plume was also observed to vary with the relative velocity between the laser scan and the cross-flow: the critical condition (when the plume is highest) occurs when the laser scan is parallel to, and in the same direction as, the cross-flow. The required flowrate for successful extraction is therefore dependent on the chosen process parameters, and must therefore be scaled accordingly if the plume is to be directed towards the chamber exit and not recirculate within the chamber.

Significant distortions due to refractive index gradients were observed when looking down through the plume at the powder bed with the direct imaging, and the associated background oriented schlieren processing. These effects increased at low cross-flow rates, due to the increased height of the laser plume above the powder bed, and extended many tens of mm beyond the processing area. The finite element model incorporating cross-flow showed that the temperature drops to ambient ~4 mm beyond the processing area, whereas appreciable Fe concentrations were predicted hundreds of mm away from the laser. Therefore, the refractive index gradients imaged away from the immediate vicinity of the melt pool are predominately due to fumes. These results suggest that the simultaneous operation of multiple lasers as well as optical process monitoring away from the melt pool can be affected by the transport of fumes. A cross-flow stream with sufficient momentum to extract and disperse fumes efficiently is therefore essential to facilitate light propagation within the atmosphere of LPBF chambers.

Acknowledgements

The authors are grateful to Tim Nicholls of Photron (Europe) Ltd. for use of the Photron Fastcam Mini AX200 camera. This work was supported by the Engineering and Physical Sciences Research Council (Grant number EP/P027415/1) and Renishaw plc.

References

[1] C. Pei, W. Zeng, H. Yuan, A damage evolution model based on micro-structural characteristics for an additive manufactured superalloy under monotonic and cyclic loading conditions, Int. J. Fatigue. (2019) 105279. https://doi.org/10.1016/j.ijfatigue.2019.105279.

[2] A. Gisario, M. Kazarian, F. Martina, M. Mehrpouya, Metal additive manufacturing in the commercial aviation industry: A review, J. Manuf. Syst. 53 (2019) 124–149. https://doi.org/10.1016/j.jmsy.2019.08.005.

[3] B. Ferrar, L. Mullen, E. Jones, R. Stamp, C.J. Sutcliffe, Gas flow effects on selective laser melting (SLM) manufacturing performance, J. Mater. Process. Technol. 212 (2012) 355–364. https://doi.org/10.1016/j.jmatprotec.2011.09.020.

[4] A. Ladewig, G. Schlick, M. Fisser, V. Schulze, U. Glatzel, Influence of the shielding gas flow on the removal of process by-products in the selective laser melting process, Addit. Manuf. 10 (2016) 1–9. https://doi.org/10.1016/j.addma.2016.01.004.

[5] A.B. Anwar, Q.-C. Pham, Selective laser melting of AlSi10Mg: Effects of scan direction, part placement and inert gas flow velocity on tensile strength, J. Mater. Process. Technol. 240 (2017) 388–396. https://doi.org/10.1016/j.jmatprotec.2016.10.015.

[6] A.M. Philo, D. Butcher, S. Sillars, C.J. Sutcliffe, J. Sienz, S.G.R. Brown, N.P. Lavery, A Multiphase CFD Model for the Prediction of Particulate Accumulation in a Laser Powder Bed Fusion Process, in: L. Nastac, K. Pericleous, A.S. Sabau, L. Zhang, B.G. Thomas (Eds.), CFD Model. Simul. Mater. Process. 2018, Springer International Publishing, 2018: pp. 65–76.

[7] A.B. Anwar, I.H. Ibrahim, Q.-C. Pham, Spatter transport by inert gas flow in selective laser melting: A simulation study, Powder Technol. 352 (2019) 103–116. https://doi.org/10.1016/j.powtec.2019.04.044.

[8] J. Reijonen, A. Revuelta, T. Riipinen, K. Ruusuvuori, P. Puukko, On the effect of shielding gas flow on porosity and melt pool geometry in laser powder bed fusion additive manufacturing, Addit. Manuf. 32 (2020) 101030. https://doi.org/10.1016/j.addma.2019.101030.

[9] A. Matsunawa, H. Yoshida, S. Katayama, Beam-plume interaction in pulsed YAG laser processing, in: Int. Congr. Appl. Lasers Electro-Opt., Laser Institute of America, Boston, Massachusetts, USA, 1984: pp. 35–42. https://doi.org/10.2351/1.5057620.

[10] P.Y. Shcheglov, A.V. Gumenyuk, I.B. Gornushkin, M. Rethmeier, V.N. Petrovskiy, Vapor–plasma plume investigation during high-power fiber laser welding, Laser Phys. 23 (2012) 016001. https://doi.org/10.1088/1054-660X/23/1/016001.

[11] P.Yu. Shcheglov, S.A. Uspenskiy, A.V. Gumenyuk, V.N. Petrovskiy, M. Rethmeier, V.M. Yermachenko, Plume attenuation of laser radiation during high power fiber laser welding, Laser Phys. Lett. 8 (2011) 475–480. https://doi.org/10.1002/lapl.201110010.

[12] P. Bidare, I. Bitharas, R.M. Ward, M.M. Attallah, A.J. Moore, Laser powder bed fusion at sub-atmospheric pressures, Int. J. Mach. Tools Manuf. 130–131 (2018) 65–72. https://doi.org/10.1016/j.ijmachtools.2018.03.007.

[13] P. Bidare, I. Bitharas, R.M. Ward, M.M. Attallah, A.J. Moore, Laser powder bed fusion in high-pressure atmospheres, Int. J. Adv. Manuf. Technol. 99 (2018) 543–555. https://doi.org/10.1007/s00170-018-2495-7.

[14] M.J. Matthews, G. Guss, S.A. Khairallah, A.M. Rubenchik, P.J. Depond, W.E. King, Denudation of metal powder layers in laser powder bed fusion processes, Acta Mater. 114 (2016) 33–42. https://doi.org/10.1016/j.actamat.2016.05.017.

[15] P. Bidare, I. Bitharas, R.M. Ward, M.M. Attallah, A.J. Moore, Fluid and particle dynamics in laser powder bed fusion, Acta Mater. 142 (2018) 107–120. https://doi.org/10.1016/j.actamat.2017.09.051.

[16] P. Bidare, R.R.J. Maier, R.J. Beck, J.D. Shephard, A.J. Moore, An open-architecture metal powder bed fusion system for in-situ process measurements, Addit. Manuf. 16 (2017) 177–185. https://doi.org/10.1016/j.addma.2017.06.007.

[17] J. Ding, P. Colegrove, F. Martina, S. Williams, R. Wiktorowicz, M.R. Palt, Development of a laminar flow local shielding device for wire+arc additive manufacture, J. Mater. Process. Technol. 226 (2015) 99–105. https://doi.org/10.1016/j.jmatprotec.2015.07.005.

[18] L. Cattafesta, C. Bahr, J. Mathew, Fundamentals of Wind-Tunnel Design, in: R. Blockley, W. Shyy (Eds.), Encycl. Aerosp. Eng., John Wiley & Sons, Ltd, Chichester, UK, 2010: p. eae532. https://doi.org/10.1002/9780470686652.eae532.

[19] I. Bitharas, N.A. McPherson, W. McGhie, D. Roy, A.J. Moore, Visualisation and optimisation of shielding gas coverage during gas metal arc welding, J. Mater. Process. Technol. 255 (2018) 451–462. https://doi.org/10.1016/j.jmatprotec.2017.11.048.

[20] G.S. Settles, Schlieren and Shadowgraph Techniques: Visualizing Phenomena in Transparent Media, Springer, 2001.
[21] A. Vogel, I. Apitz, S. Freidank, R. Dijkink, Sensitive high-resolution white-light Schlieren technique with a large dynamic range for the investigation of ablation dynamics, Opt. Lett. 31 (2006) 1812. https://doi.org/10.1364/OL.31.001812.
[22] Renishaw plc, Data sheet: SS 316L-0407 powder for additive manufacturing, (2017).
[23] Y. Cressault, A.B. Murphy, P. Teulet, A. Gleizes, M. Schnick, Thermal plasma properties for Ar–Cu, Ar–Fe and Ar–Al mixtures used in welding plasmas processes: II. Transport coefficients at atmospheric pressure, J. Phys. Appl. Phys. 46 (2013) 415207. https://doi.org/10.1088/0022-3727/46/41/415207.
[24] C.S. Kim, Thermophysical properties of stainless steels, Argonne National Lab. (USA), 1975.
[25] R.C. Flagan, M.M. Lunden, Particle structure control in nanoparticle synthesis from the vapor phase, Mater. Sci. Eng. A. 204 (1995) 113–124. https://doi.org/10.1016/0921-5093(95)09947-6.
[26] S. Traore, M. Schneider, I. Koutiri, F. Coste, R. Fabbro, C. Charpentier, P. Lefebvre, P. Peyre, Influence of gas atmosphere (Ar or He) on the laser powder bed fusion of a Ni-based alloy, J. Mater. Process. Technol. (2020) 116851. https://doi.org/10.1016/j.jmatprotec.2020.116851.
[27] S. Ly, A.M. Rubenchik, S.A. Khairallah, G. Guss, M.J. Matthews, Metal vapor micro-jet controls material redistribution in laser powder bed fusion additive manufacturing, Sci. Rep. 7 (2017) 1–12. https://doi.org/10.1038/s41598-017-04237-z.
[28] C. Zhao, K. Fezzaa, R.W. Cunningham, H. Wen, F. De Carlo, L. Chen, A.D. Rollett, T. Sun, Real-time monitoring of laser powder bed fusion process using high-speed X-ray imaging and diffraction, Sci. Rep. 7 (2017) 3602. https://doi.org/10.1038/s41598-017-03761-2.
[29] Q. Guo, C. Zhao, L.I. Escano, Z. Young, L. Xiong, K. Fezzaa, W. Everhart, B. Brown, T. Sun, L. Chen, Transient dynamics of powder spattering in laser powder bed fusion additive manufacturing process revealed by in-situ high-speed high-energy x-ray imaging, Acta Mater. 151 (2018) 169–180. https://doi.org/10.1016/j.actamat.2018.03.036.
[30] A.R. Nassar, M.A. Gundermann, E.W. Reutzel, P. Guerrier, M.H. Krane, M.J. Weldon, Formation processes for large ejecta and interactions with melt pool formation in powder bed fusion additive manufacturing, Sci. Rep. 9 (2019) 1–11. https://doi.org/10.1038/s41598-019-41415-7.
[31] T.J. Atherton, D.J. Kerbyson, Size invariant circle detection, Image Vis. Comput. 17 (1999) 795–803. https://doi.org/10.1016/S0262-8856(98)00160-7.
[32] M.J. Hargather, G.S. Settles, Natural-background-oriented schlieren imaging, Exp. Fluids. 48 (2010) 59–68. https://doi.org/10.1007/s00348-009-0709-3.
[33] T.J. Rockstroh, J. Mazumder, Spectroscopic studies of plasma during cw laser materials interaction, J. Appl. Phys. 61 (1987) 917. https://doi.org/10.1063/1.338142.
[34] C.J. Knight, Theoretical Modeling of Rapid Surface Vaporization with Back Pressure, AIAA J. 17 (1979) 519–523. https://doi.org/10.2514/3.61164.
[35] Y.A. Mayi, M. Dal, P. Peyre, M. Bellet, C. Metton, C. Moriconi, R. Fabbro, Laser-induced plume investigated by finite element modelling and scaling of particle entrainment in laser powder bed fusion, J. Phys. Appl. Phys. 53 (2020) 075306. https://doi.org/10.1088/1361-6463/ab5900.
[36] M. Simonelli, C. Tuck, N.T. Aboulkhair, I. Maskery, I. Ashcroft, R.D. Wildman, R. Hague, A Study on the Laser Spatter and the Oxidation Reactions During Selective Laser Melting of 316L Stainless Steel, Al-Si10-Mg, and Ti-6Al-4V, Metall. Mater. Trans. A. 46 (2015) 3842–3851. https://doi.org/10.1007/s11661-015-2882-8.

Graphical abstract

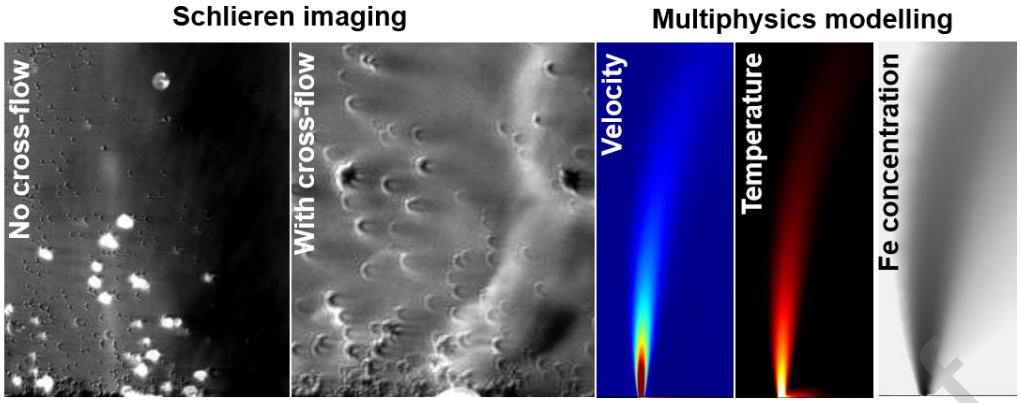

CRediT author statement

Ioannis Bitharas: Conceptualization, Methodology, Software, Formal analysis, Investigation , Writing - Original Draft, Writing – Review & Editing, Visualization **Alex Burton:** Conceptualization, Software, Investigation **Alex Ross:** Investigation, Resources **Andrew J Moore:** Methodology, Validation, Resources, Writing - Original Draft, Writing - Review & Editing, Supervision, Project administration, Funding acquisition

Declaration of interests

☒ The authors declare that they have no known competing financial interests or personal relationships that could have appeared to influence the work reported in this paper.

☐The authors declare the following financial interests/personal relationships which may be considered as potential competing interests: